

# Online Adaptation for Implicit Object Tracking and Shape Reconstruction in the Wild

Jianglong Ye<sup>1\*</sup> Yuntao Chen<sup>2</sup> Naiyan Wang<sup>2</sup> Xiaolong Wang<sup>1</sup>  
UCSD<sup>1</sup> TuSimple<sup>2</sup>

j7ye@ucsd.edu, chenYuntao08@gmail.com, winsty@gmail.com, xiw012@ucsd.edu

## Abstract

Tracking and reconstructing 3D objects from cluttered scenes are the key components for computer vision, robotics and autonomous driving systems. While recent progress in implicit function (e.g., DeepSDF) has shown encouraging results on high-quality 3D shape reconstruction, it is still very challenging to generalize to cluttered and partially observable LiDAR data. In this paper, we propose to leverage the continuity in video data. We introduce a novel and unified framework which utilizes a DeepSDF model to simultaneously track and reconstruct 3D objects in the wild. We online adapt the DeepSDF model in the video, iteratively improving the shape reconstruction while in return improving the tracking, and vice versa. We experiment with both Waymo and KITTI datasets, and show significant improvements over state-of-the-art methods for both tracking and shape reconstruction.

## 1. Introduction

Recent development on implicit function has shown a tremendous success on high-quality 3D shape reconstruction [7, 29, 33, 5, 23]. Among them, DeepSDF [33] is a representative work which uses a deep auto-decoder which takes a shape code and a coordinate as inputs to predict the signed distance to the shape surface. However, it usually relies on pre-training on dense synthetic data (e.g., ShapeNet [6], ScanNet [9]) to obtain category level prior, and then finetune it to adapt to new instance. How to collect such large-scale high quality dense data becomes a burden to apply DeepSDF.

On the other hand, with the development of 3D sensing technologies, 3D point cloud video sequences become cheap and feasible. Nevertheless, in such data, the object of interest in each frame is much sparser than that in the synthetic dataset due to viewing angle or distance. DeepSDF could hardly be applied directly on each single frame, since even with the learned prior, it either reconstructs close to mean

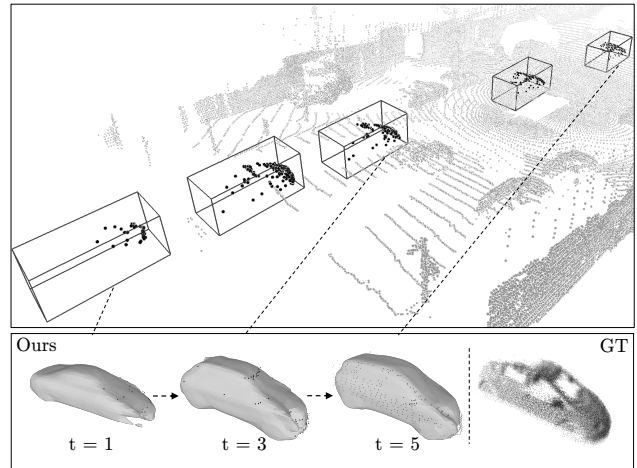


Figure 1: **3D object tracking and shape reconstruction.** We propose a novel framework to utilize DeepSDF to perform tracking and reconstruction simultaneously. We visualize five time steps of tracking and three reconstructed shapes. We obtain better and better shape close to the ground-truth point clouds over time, which in return helps the tracking.

shape or overfits to the noise given partial observations and the artifacts around. Fortunately, multi-frame data could make up this intrinsic defects, but calls for a robust algorithm that could jointly discover the poses of objects in each frame and utilize them for a better shape reconstruction.

In this paper, instead of taking object tracking and shape reconstruction as two separate tasks, we propose to solve them collaboratively using one single model. Specifically, we utilize the tracked poses of objects to update the DeepSDF codes, while the DeepSDF shape helps tracking in challenging cases such as sparse or occluded observations. Our framework iterates between object tracking and online adaptation along the video to improve performance for both tasks. As shown in Figure 1, the reconstructed shape improves progressively as more frames are tracked.

To track with DeepSDF, we first optimize the shape code via back-propagation using the localized partial point clouds

\*This work is complete during the first author’s internship at TuSimple.

given in the initial time step. While the shape code itself might not give perfect reconstruction, it offers a shape prior to construct a complete signed distance field of the object as a template. We then perform object tracking via optimizing a differentiable template matching process. Specifically, given the current model and point clouds in a new time step, we apply a 3D transformation on the partial point clouds (3D translation and rotation) and feed them to the DeepSDF model to compute their signed distances. If the 3D transformation is correct, the distance should be close to zero. We then optimize the absolute distance via back-propagation. Since the 3D transformation operation is differentiable, we can back-propagate the gradients through the point clouds to adjust the transformation. Once the object point clouds are localized with the correct pose, we can then use the point clouds to optimize the shape code.

We conduct our experiments with LiDAR video data recorded in the wild. Our DeepSDF model is first trained in the ShapeNet [6] dataset to obtain the shape prior. We then perform online adaptation with the model on both Waymo [44] and KITTI [17] datasets. We demonstrate that our method not only achieves state-of-the-art performance on 3D object tracking in both datasets, but also improves shape reconstruction at the same time.

We highlight our main contributions as follows:

- We propose a novel framework for simultaneous tracking and shape reconstruction and boost the performances of both.
- We introduce the learning-based implicit function with its shape prior to this joint task for the first time.
- Our method achieves the state-of-the-art performance in 3D single object tracking, while also improves the performance of shape reconstruction.

## 2. Related Work

**Implicit neural representations.** In the past few years, a lot of advances have been made in 3D representation learning with meshes [2, 46, 10], point clouds [35, 50, 1] and voxel grids [48, 8, 20]. Recently, the learning-based implicit functions have shown promising results on high-quality 3D shape reconstruction [33, 29, 7, 21, 49, 37, 38, 18, 25, 42, 31, 30, 41, 45]. For example, Mescheder et al. [29] proposed the Occupancy network which learns to predict whether a 3D point is inside or outside the object given the 3D point cloud or image inputs. Saito et al. [37] further extended this work with local feature encoding beyond global shape features. Both of these approaches adopt an encoder-decoder architecture which reconstruct the shape in a feed-forward pass. In parallel, Park et al. [33] introduced an auto-decoder DeepSDF for learning the signed distance to the shape surfaces. Instead of one forward pass, DeepSDF offers a shape code to optimize during inference and achieve better generalization on unseen instances. Based on this observation,

Shivam et al. [12] introduced good practices on generalizing DeepSDF to point cloud data in-the-wild.

**3D object tracking.** There are two paradigms for 3D object tracking. The first paradigm adopts a model-based tracking-by-detection strategy [47, 40, 28, 39, 3] which utilizes an off-the-shelf detector [26, 34] to localize the objects in each time step, and then associate the objects across frames for tracking. However, the performance of these methods highly relies on the detection algorithm and the temporal continuity in video data is not well explored. The second paradigm is model-free. It leverages the tracking results in previous frames and their similarities to the current frame for tracking [19, 22, 52, 36, 14]. For example, Giancola et al. [19] first proposed to apply a Siamese network in 3D for matching and exploit a shape completion network for regularization. To improve the speed for searching candidate boxes in each frame, Zarzar et al. [52] applied a 2D Siamese network to generate coarse search candidates. While these approaches demonstrate their effectiveness, they still require annotations in the video sequences to train the model. On the other hand, our method is annotation free except for the first frame. It directly adapts a model trained on synthetic data online for tracking. In this sense, our method is closely related to the setting in [32] where a new LiDAR-SOT tracking benchmark is tackled by a point cloud registration approach. Instead of directly matching between point clouds, our method utilizes the shape prior refined in each time step for better tracking.

**Joint pose estimation and shape reconstruction.** Our work is closely related to recent advances on joint estimation of 3D object pose and shape [53, 13, 27, 4, 24, 43, 16, 51]. For example, Zeeshan et al. [53] estimated the 3D wireframe models of multiple objects within a scene, which leads to higher performance in both object localization and viewpoint estimation. Kundu et al. [27] adopted PCA on TSDF volume to represent object shape and train a 3D-RCNN to regress both 3D poses and shape parameters in a single forward pass. Instead of estimating object pose and shape in a single frame, Feng et al. [16] utilized semantic mesh keypoints and segmentation masks to recover poses and shapes of cars in videos. To the best of our knowledge, our method is the first work using implicit function to simultaneously track 3D object and recover poses and shape on in-the-wild videos.

## 3. Method

### 3.1. Pipeline

Our method consists of three components: shape initialization, pose estimation and shape adaptation. At the beginning of single object tracking, a 3D bounding box of the object with pose  $\mathbf{T} \in SE(3)$  and size  $\mathbf{b} = \{h, w, l\} \in \mathbb{R}^3$  (height, width and length) are provided as the tracking tem-

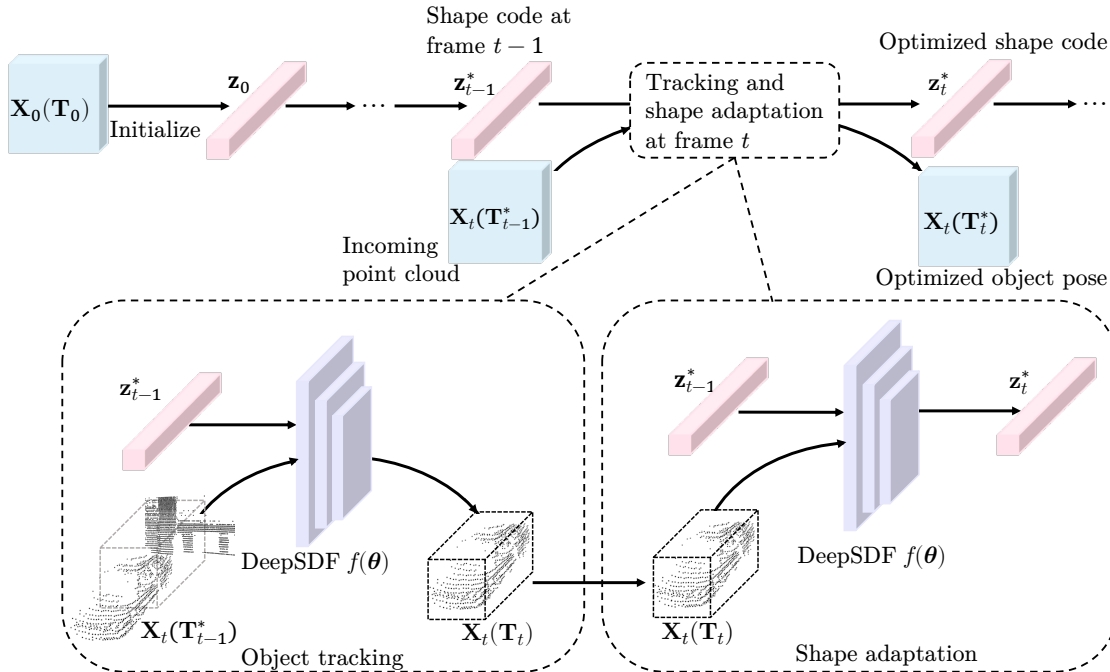


Figure 2: **Overview of our method.** After initialization of the shape code, tracking and shape adaptation are performed iteratively. At a specific frame, the incoming object point cloud is first aligned to the previous shape, and then the shape is adapted to the aligned point cloud. Both procedures are based on DeepSDF.

plate.<sup>1</sup> Note that, similar to mainstream 3D detection and tracking benchmarks, object pose here only consists of yaw and translation. We use  $\mathbf{X}(\mathbf{T}) = \{\mathbf{x} | \mathbf{T}\mathbf{x} \leq \mathbf{b}, \mathbf{x} \in \mathbf{P}\}$  to denote LiDAR points  $\mathbf{x}$  in frame  $\mathbf{P}$  that are inside the 3D bounding box. We omit  $\mathbf{b}$  for simplicity as the dimension of object is known and fixed. As shown in Figure 2, we first initialize the shape with aligned point cloud at first frame, then in each frame we iterate between aligning the incoming object points  $\mathbf{X}(\mathbf{T})$  with reconstructed shape and adapting the shape from previous tracked point clouds  $\{\mathbf{X}_0(\mathbf{T}_0^*), \mathbf{X}_1(\mathbf{T}_1^*), \dots, \mathbf{X}_t(\mathbf{T}_t^*)\}$  with optimal poses  $\{\mathbf{T}_0^*, \mathbf{T}_1^*, \dots, \mathbf{T}_t^*\}$ .

### 3.2. Implicit Function for Shape Representation

Vehicles in the wild come with a wide variation of shapes and partial observations as shown in Figure 1, which introduces challenges to the use of fixed shape models of car [13, 24]. Consequently, we choose DeepSDF [33] as our shape representation for its expressiveness and flexibility. The continuous nature of DeepSDF allows our method to optimize object pose smoothly via back-propagation.

Signed distance function(SDF) is a widely used representation for 3D shape. SDF maps the spatial coordinates of a

point  $\mathbf{x}$  to its signed distance  $s$  to the closest surface.

$$SDF(\mathbf{x}) = s, \quad \mathbf{x} \in \mathbb{R}^3, s \in \mathbb{R}. \quad (1)$$

DeepSDF  $f$  is a coordinate-based MLP parameterized by  $\theta$  which approximates the SDF. It takes both 3D coordinates  $\mathbf{x}$  and a learnable per-object shape code  $\mathbf{z}$  as inputs. The DeepSDF function can be represented as,

$$f(\mathbf{x}, \mathbf{z}; \theta) = s, \quad \mathbf{x} \in \mathbb{R}^3, \mathbf{z} \in \mathbb{R}^d, s \in \mathbb{R}, \quad (2)$$

which encodes a one-to-one mapping between shape code  $\mathbf{z}$  and 3D shape, and shape representation for different objects can be achieved by optimizing the shape code for each object, while leaving the parameters of MLP  $\theta$  fixed.

In our method, we first pre-train the deepSDF network using the *car* category of the ShapeNet Core [6] dataset. Then, given the initial pose  $\mathbf{T}_0$ , the corresponding optimal code (a.k.a shape representation)  $\mathbf{z}_0^*$  could be obtained by

$$\mathbf{z}_0^* = \arg \min_{\mathbf{z}} \sum_{\mathbf{x} \in \mathbf{X}_0(\mathbf{T}_0^*)} \text{smooth\_l1}(f(\mathbf{x}, \mathbf{z}; \theta), 0) + \lambda \|\mathbf{z}\|_2^2. \quad (3)$$

An  $\ell_2$  regularizer is applied for the shape code  $\mathbf{z}$  to prevent over-fitting. Generally, points in a LiDAR scan come from the surface of objects, where the SDF values are 0.

<sup>1</sup>For all symbols used in this work, please refer to supplementary materials.

### 3.3. Joint Tracking and Shape Reconstruction in the Wild

Different from standalone shape reconstruction where dense surface points of objects are already well-posed in the canonical view, our setting requires joint pose estimation and shape estimation, making it far more challenging.

Our joint tracking and shape reconstruction problem consists of three terms: The first is the SDF loss function, while the second is the regularization of the shape code to alleviate overfitting issue caused by partial view and noisy points. And the last one is the point cloud registration loss to capture fine-grained details. For frame  $t$ , we have:

$$\min_{\mathbf{T}, \mathbf{z}} \sum_{\mathbf{x} \in \mathbf{H}_t \cup \mathbf{X}_t(\mathbf{T})} \text{smooth\_ll}(f(\mathbf{x}, \mathbf{z}; \boldsymbol{\theta}), 0) + \lambda \|\mathbf{z}\|_2^2 + \gamma \phi(\mathbf{X}_t(\mathbf{T}), \mathbf{H}_t), \quad (4)$$

where  $\mathbf{H}_t$  stands for points from all previously tracked objects, which is defined as:

$$\mathbf{H}_t = \Gamma(\{\mathbf{X}_0(\mathbf{T}_0^*) \cup \mathbf{X}_1(\mathbf{T}_1^*) \cup \dots \cup \mathbf{X}_{t-1}(\mathbf{T}_{t-1}^*)\}), \quad (5)$$

and  $\Gamma: \mathbf{X} \rightarrow 2^{\mathbf{X}}$  selects which subset of historical points are used in optimization. At each time step, there are multiple choices of the subset: the previous frame observation, the combination of the first frame observation and previous frame observation, and all previous observations. We compare different choices in Table 3.

Here  $\phi(\mathbf{X}_t(\mathbf{T}), \mathbf{H}_t) = \sum_{\mathbf{x} \in \mathbf{X}_t(\mathbf{T})} \min_{\mathbf{y} \in \mathbf{H}_t} \|\mathbf{x} - \mathbf{y}\|_2^2$  is the single-side Chamfer distance loss. The Chamfer distance loss between the object points in current frame and aggregated object points from previous time steps helps the pose estimation capture finer details of the object shape, as reconstructed shapes are tend to be over-smoothed.

Directly solving Eq. 4 leads to sub-optimal results in practice as the pose  $\mathbf{T}$  and the shape code  $\mathbf{z}$  are two sets of variables with different scales and loss surfaces. Instead, we take an iterative optimization approach as described in Algorithm 1 and Figure 2 to ease the difficulty of optimization. Specifically, our approach iterates between the **object tracking** task and **shape adaptation** task described as following.

**Object Tracking:** To perform tracking, we fix the optimal shape code  $\mathbf{z}_{t-1}^*$  obtained from the last frame, and optimize the object pose  $\mathbf{T}_t$  as:

$$\mathbf{T}_t^* = \arg \min_{\mathbf{T}} \gamma \phi(\mathbf{X}_t(\mathbf{T}), \mathbf{H}_t) + \sum_{\mathbf{x} \in \mathbf{X}_t(\mathbf{T})} \text{smooth\_ll}(f(\mathbf{x}, \mathbf{z}_{t-1}^*; \boldsymbol{\theta}), 0), \quad (6)$$

which is actually Eq. 4 with  $\mathbf{z}$  fixed. We visualize the tracking process based on Eq. 6 in Figure 3a. Initially, the point clouds are in the areas (the yellow zone) with high signed

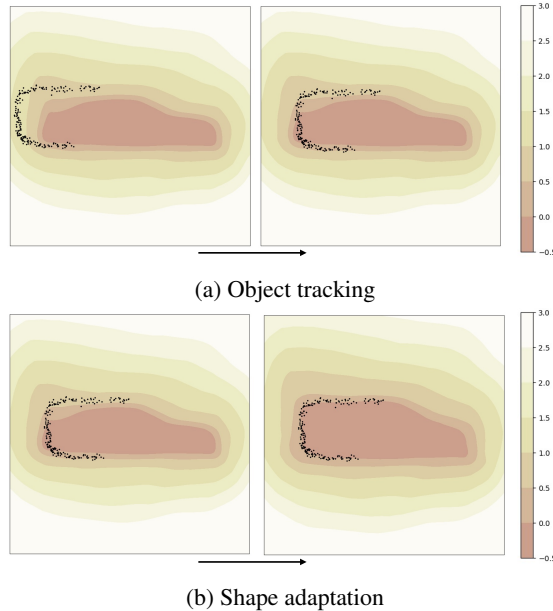


Figure 3: **Iterative optimization.** We optimize pose by pushing the point cloud to the zero-level set of the SDF field in (a), and deform the SDF field to match the point cloud in (b) for better shape. We use different temperature of the color to represent the distances from the surface.

---

#### Algorithm 1 Pipeline

---

**Input:** LiDAR scans  $\mathbf{P}_{0:t}$ , initial object pose  $\mathbf{T}_0$ , object size  $\mathbf{b}$ , DeepSDF  $f$  with parameters  $\boldsymbol{\theta}$

**Output:** Subsequent object poses:  $\mathbf{T}_{1:t}$ , shape code  $\mathbf{z}$

- 1: Extract object points with initial pose and fixed object size:  $\mathbf{X}_0(\mathbf{T}_0) \leftarrow \{\mathbf{x} | \mathbf{T}_0 \mathbf{x} \leq \mathbf{b}, \mathbf{x} \in \mathbf{P}_0\}$ .
  - 2: Initialize shape code  $\mathbf{z}_0$  by solving Eq. 3 with  $\mathbf{X}_0(\mathbf{T}_0)$  and  $f(\boldsymbol{\theta})$
  - 3: Frame number  $t \leftarrow 1$
  - 4: **while** not the end of tracking **do**
  - 5:   Extract object points with optimized pose at previous frame:  $\mathbf{X}_t(\mathbf{T}_{t-1}^*) \leftarrow \{\mathbf{x} | \mathbf{T}_{t-1}^* \mathbf{x} \leq \mathbf{b}, \mathbf{x} \in \mathbf{P}_t\}$
  - 6:   Estimate object pose  $\mathbf{T}_t^*$  by solving Eq. 6 with  $\mathbf{X}_t(\mathbf{T}_{t-1}^*)$ ,  $\mathbf{z}_{t-1}^*$  and  $f(\boldsymbol{\theta})$ .
  - 7:   Update shape code  $\mathbf{z}_t^*$  by solving Eq. 7 with  $\mathbf{X}_t(\mathbf{T}_t^*)$  and  $f(\boldsymbol{\theta})$ .
  - 8:    $t \leftarrow t + 1$
  - 9: **end while**
- 

distance. By optimizing Eq. 6, we push the point clouds towards the zero-level set (i.e., the surface of the shape template, boundary of the red zone). When optimizing the object pose, the loss weights of translation and rotation are equal.

**Shape Adaptation:** After aligning the point clouds, we adapt the shape utilizing observations to improve the shape quality. Specifically, we align the shape and the historical observations by minimizing the distances between them. The

shape adaptation is achieved via optimizing the shape code,

$$\mathbf{z}_t^* = \arg \min_{\mathbf{z}} \sum_{\mathbf{x} \in \mathbf{H}_{t+1}} \text{smooth\_l1}(f(\mathbf{x}, \mathbf{z}; \boldsymbol{\theta}), 0) + \lambda \|\mathbf{z}\|_2^2, \quad (7)$$

which is Eq. 4 with  $\mathbf{T}$  fixed. We visualize the shape adaptation based on Eq. 7 in Figure 3b. Specifically, given the tracked object location and pose, we deform the SDF field so that we push the boundary of the zero-level set (the boundary of the red zone) towards the point clouds. In return, this fine-tuned shape code could serve as a prior for tracking.

**Detection Loss:** Since our method does not require training on a specific dataset, it does not take advantage of human annotation. To leverage the information of the annotated bounding box, we can optionally incorporate an off-the-shelf detector. Specifically, we first select the closest detection result within a threshold of 3m as the corresponding predicted pose  $\mathbf{T}_{det}$ . Then we add a detection loss to minimize the difference between our estimated pose and the corresponding pose of detection. If there is no such detection box exists, then the detection loss is discarded. With the detection term, the Eq. 6 for object tracking becomes:

$$\mathbf{T}_t^* = \arg \min_{\mathbf{T}} \gamma \phi(\mathbf{X}_t(\mathbf{T}), \mathbf{H}_t) + \text{l1}(\mathbf{T}, \mathbf{T}_{det}) + \sum_{\mathbf{x} \in \mathbf{X}_t(\mathbf{T})} \text{smooth\_l1}(f(\mathbf{x}, \mathbf{z}_{t-1}^*; \boldsymbol{\theta}), 0). \quad (8)$$

## 4. Experiments

We conduct experiments on the Waymo open dataset [44] and the KITTI tracking dataset [17] to evaluate both object tracking and shape reconstruction. We also perform thorough ablation studies to demonstrate how tracking and reconstruction can contribute to each other using online adaptation.

### 4.1. Experimental Settings

**Pre-training.** For the pre-training of DeepSDF model, we use 2364 synthetic objects from the ‘‘car’’ category of the ShapeNet Core [6] dataset. Since we aim to recover object shapes from partial observations, we simulate partial point clouds from LiDAR scan and use the complete SDF samples as the supervision of our DeepSDF model. For the input, we randomly select 24 poses around each object which are 4-10 meters away from the object. Based on selected poses, we sample partial point clouds on the mesh surface with the ray casting algorithm. For the supervision, we directly employ the processed SDF samples provided by DISN [49].

**Datasets.** For tracking on the Waymo dataset, we follow the protocol in LiDAR-SOT [32], which utilizes 1121 tracklets that are longer than 100 frames and have more than 20 points in the first 10 frames. Besides, the dataset is split into easy, medium, and hard subsets based on the number of points in the first frame of each tracklet. We also follow

LiDAR-SOT [32] to remove the ground points to improve the performance. For tracking on the KITTI dataset, we follow the settings in SC3D[19]. Since we do not need to train on KITTI, we only use scenes 17-18 from all 21 scenes for validation, 19-20 for testing.

**Evaluation metrics.** To evaluate the shape reconstruction, we aggregate point clouds from all frames of each tracklet using the annotated bounding boxes as pseudo-ground-truth shapes. Since the ground-truth aggregated points are not complete, we adopt Asymmetric Chamfer Distance (ACD) to measure the shape fidelity. The ACD is defined as the mean squared distance from each ground-truth point to the nearest surface point on the reconstructed shape. In addition, we calculate the recall at threshold  $t$ . The recall is defined as the fraction of ground-truth aggregated points within  $t$  of a predicted point. In the paper, we set threshold  $t = 0.2m$ .

For single object tracking, we adopt the Success and Precision metrics from SC3D[19]. We add the Accuracy and Robustness metrics from [32] for Waymo dataset.

**Implementation details.** We adapt DeepSDF as our shape model by reducing the MLP from 7 layers to 5 layers and remove the final  $\tanh$ . The dimension of the latent shape code is 512. For the pre-training of DeepSDF, we use the Adam optimizer with an initial learning rate of  $1 \times 10^{-4}$  with batch size of 128. During joint tracking and reconstruction, we use SGD optimizer to optimize both object pose and shape code. The initial learning rates for pose estimation and shape code optimization are 0.1 and  $1 \times 10^{-3}$ , respectively. The numbers of iterations for pose estimation and shape code optimization are 300 and 20, respectively. In all experiments, the weight of regularization term  $\lambda$  in Eq.7 is set to 10, and the weight of chamfer distance loss  $\gamma$  in Eq.6 is set to 0.1.

Since the effect of online adaptation highly relies on the quality of the observations, it is necessary to filter out the poor quality observations. Thus we do not update the shape if the number of point in the frame is less than 10.

### 4.2. Comprehensive Comparisons

**Evaluations on Waymo.** We compare our method with SOTracker, a recent single 3D object tracking method. As shown in Table 1, our method achieves comparable results on the easy subset and outperforms SOTracker by a large margin on the hard subset. It is reasonable that shape reconstruction is more beneficial in the case of more sparse point clouds, since the shape provides a global description of the object, thus is not prone to the error of partial and incomplete view.

We also evaluate the performance of the shape reconstruction. Since shapes are represented by aggregated point clouds in SOTracker, metrics including ACD and Recall are not suitable, we first aggregate point clouds based on the predicted pose and then exploit our SDF model to convert the point clouds to mesh for comparison. As shown in Table 1, our method outperforms the baseline on every subset. This

Method	All		Easy		Medium		Hard	
	Succ $\uparrow$	Prec $\uparrow$						
SOTracker [32]	57.4	64.9	69.4	<b>75.7</b>	53.6	60.7	47.1	56.5
Ours	<b>62.3</b>	<b>65.7</b>	<b>71.5</b>	74.1	<b>58.8</b>	<b>61.8</b>	<b>54.9</b>	<b>59.9</b>

Method	All		Easy		Medium		Hard	
	Acc $\uparrow$	Rob $\uparrow$						
SOTracker [32]	57.1	50.0	69.2	<b>64.5</b>	53.2	45.1	46.6	37.8
Ours	<b>62.4</b>	<b>54.1</b>	<b>70.0</b>	63.8	<b>59.8</b>	<b>50.4</b>	<b>55.9</b>	<b>46.9</b>

Method	All		Easy		Medium		Hard	
	ACD $\downarrow$	Recall $\uparrow$						
SOTracker [32]	2.81	82.25	2.49	84.51	2.87	82.31	3.09	79.92
Ours	<b>2.50</b>	<b>84.71</b>	<b>2.30</b>	<b>86.40</b>	<b>2.76</b>	<b>83.78</b>	<b>2.44</b>	<b>83.98</b>

Table 1: **Quantitative evaluation of on the Waymo dataset.** From top to bottom, we present 1. comparison of tracking performance under Success and Precision metrics, 2. comparison of tracking performance under Accuracy and Robustness metrics, and 3. comparison of shape reconstruction performance under ACD and Recall metrics.  $\uparrow(\downarrow)$  means the performance is better with larger (smaller) values.

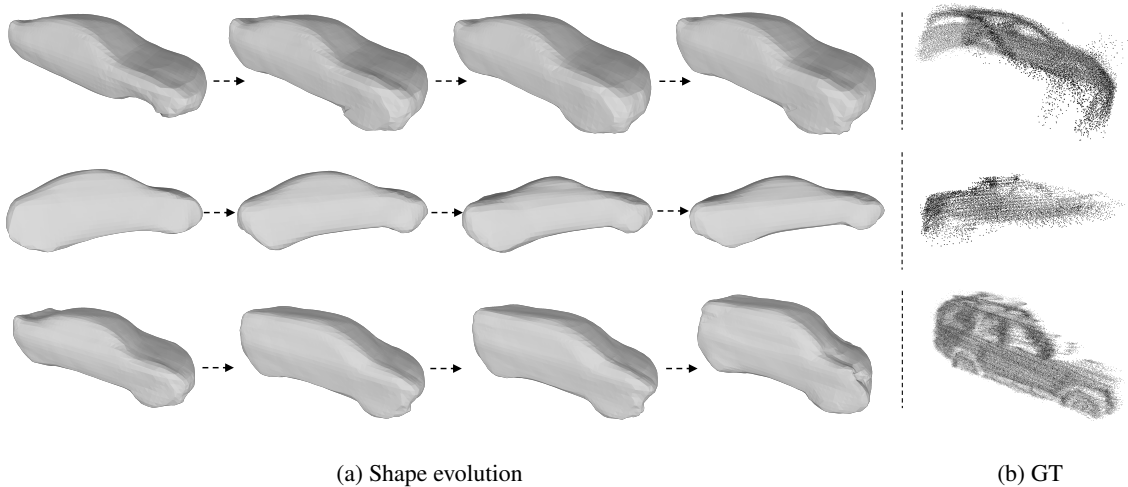


Figure 4: **Shape evolution on the Waymo dataset.** In (a), from left to right is the results of shape reconstruction at different tracking steps. The ground-truth aggregated point clouds are shown in (b). The shapes are become more and more aligned with ground-truth point clouds via online adaptation.

Method	Succ $\uparrow$	Prec $\uparrow$	ACD $\downarrow$	Recall $\uparrow$
SC3D [19]	41.3	57.9	1.68	88.56
P2B [36]	56.2	72.8	1.46	91.08
3D-SiamRPN [15]	58.2	76.2	/	/
BAT [54]	60.5	77.7	/	/
Ours	<b>62.3</b>	<b>77.7</b>	<b>1.30</b>	<b>92.50</b>

Table 2: **Quantitative evaluation on the KITTI dataset.** We outperform SC3D and P2B both in tracking (Success and Precision) and shape reconstruction (ACD and Recall).

experiment demonstrates that joint tracking and shape reconstruction leads to better performance than tracking followed by shape reconstruction.

**Evaluations on KITTI.** We further evaluate our method on the KITTI dataset. We compare our method with SC3D[19], P2B[36], 3D-SiamRPN[15] and BAT[54], which are the recent single object tracking methods on the KITTI dataset. Since all methods employ the annotated bounding box for training while our method only pretrains on ShapeNet, we employ the detection term defined in Eq. 8 on the KITTI dataset. Specifically, we utilize the predicted bounding box provided by VoxelRCNN [11].

As shown in Table 2, our method outperforms SC3D, P2B and 3D-SiamRPN and achieve comparable performance with the state-of-the-art method BAT. Similarly, we aggregate point clouds and convert them to mesh to evaluate the performance of the shape reconstruction. Once again, we demonstrate the advantages of joint tracking and shape re-

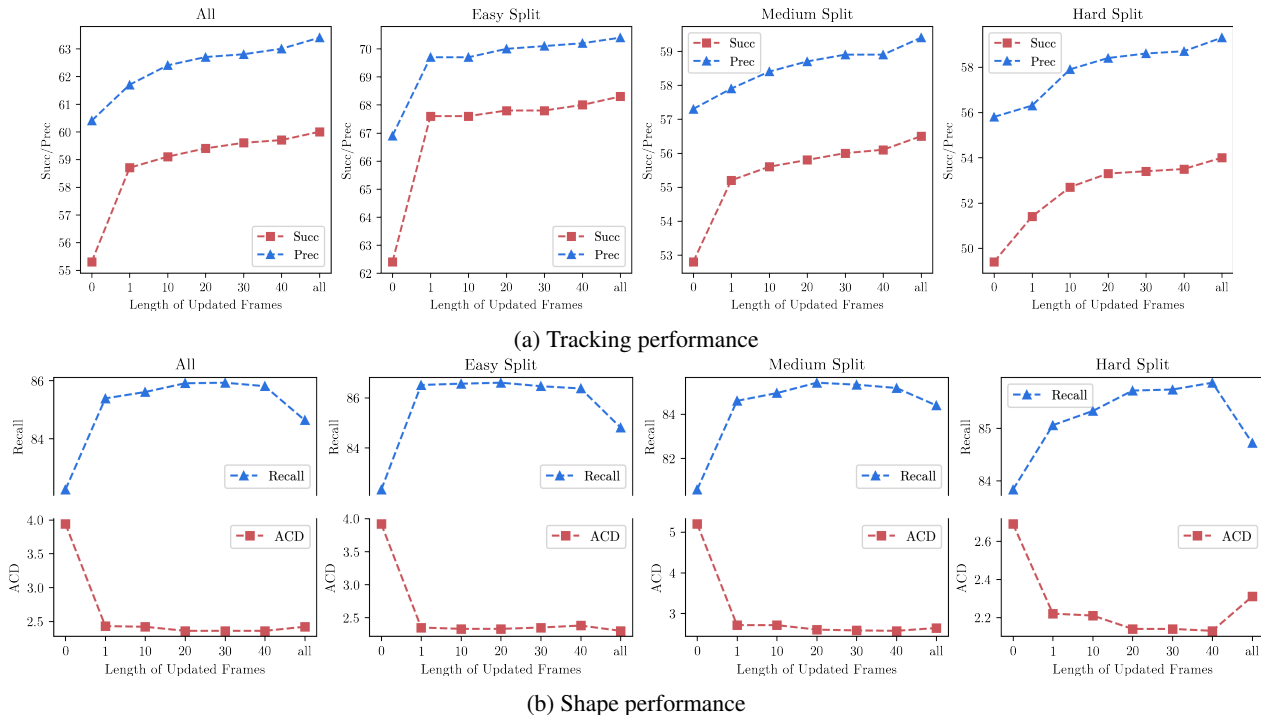


Figure 5: **Effectiveness of online adaptation mechanisms.** Due to the online adaptation mechanism, both tracking(a) and reconstruction(b) performance could be boosted.

Method	All		Easy		Medium		Hard	
	Succ $\uparrow$	Prec $\uparrow$						
Prev PC	62.3	65.7	71.6	74.2	58.3	61.5	55.2	60.2
Init PC & Prev PC	62.1	65.5	71.7	74.1	58.6	61.6	54.4	59.3
Agg PC	62.3	65.7	71.5	74.1	58.8	61.8	54.9	59.9

Table 3: **Selector function.** The results of different selector functions  $\Gamma$  in Eq. 7 on the Waymo dataset.

construction.

### 4.3. Ablation Study

**Effectiveness of online adaptation mechanisms.** To demonstrate the effectiveness of the online adaptation mechanism, we only adapt the shape in the first several frames of different lengths starting at each tracklet and fix the shape code in all subsequent frames. Then we compare the performance of tracking and reconstruction. We conduct this experiment on the Waymo dataset and exploit only shape loss for tracking and reconstruction. Besides, we extract the mean shape from ShapeNet and perform tracking with it (denoted as updating 0 frame in the figure).

As shown in Figure 5a, the tracking metric on the Waymo dataset continues to improve as the number of adapted frames increases. Similarly, we evaluate the performance of shape reconstruction in the case of different numbers of update frames. As shown in in Figure 5b, online adaptation also improves the quality of the shape. Figure 4 illustrates

our shape evolution during tracking process on the Waymo dataset. We also find that as the number of updates increases, the gains for tracking and reconstruction become saturated.

**Selector function.** Here we report results with three different selector functions: the previous frame observation (Prev PC), the combination of the first frame observation and previous frame observation (Init PC & Prev PC), and all previous observations (Agg PC). Note that the selector function refers to which point cloud we use to update the shape code at each time step, and all choices actually aggregate history information as the tracking proceeds, since the history information are encoded in the adapted shape code. We conduct experiments on the Waymo dataset and Table 3 reports the results. We observe similar results for different selection functions and our method is robust across different selection strategies.

**Ablation study.** We conduct thorough ablation studies on the Waymo and the KITTI datasets. We report our results in Table 4 and Table 5. We ablate the regularizer ( $\ell_2$  regularizer

Method	All		Easy		Medium		Hard	
	Succ $\uparrow$	Prec $\uparrow$						
w/o regularizer	58.1	61.3	67.8	70.0	53.6	56.5	51.3	56.2
w/o CD loss	60.0	63.4	68.3	70.4	56.5	59.3	54.0	59.3
w/o shape loss	42.2	42.4	57.5	57.8	34.2	34.0	32.4	33.1
full model	<b>62.3</b>	<b>65.7</b>	<b>71.5</b>	<b>74.1</b>	<b>58.8</b>	<b>61.8</b>	<b>54.9</b>	<b>59.9</b>

Table 4: **Ablation study on the Waymo dataset.** We analyze the contributions of the regularizer, the Chamfer distance loss and the shape loss.

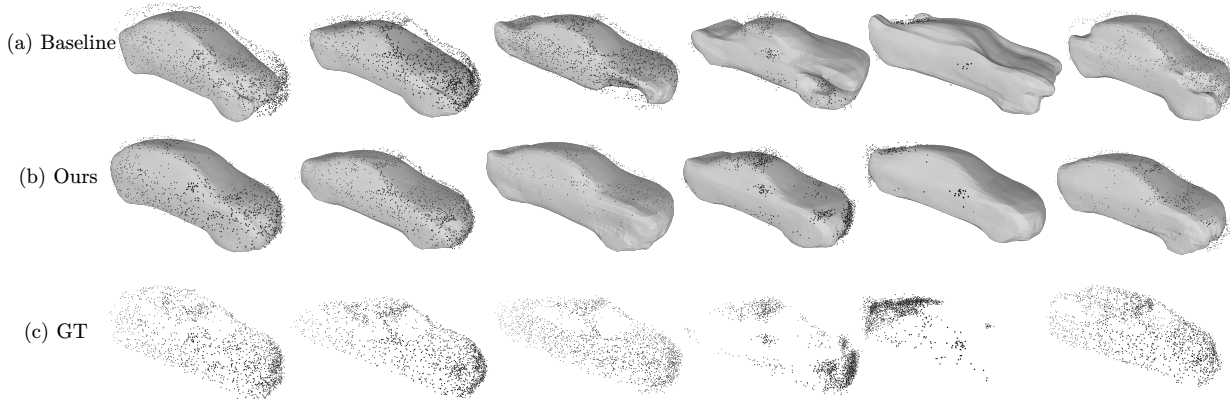


Figure 6: **Reconstructed shape on the Waymo dataset.** Our method produces more accurate shape than the baseline. The ground-truth aggregated point clouds are shown in (c).

Method	Succ $\uparrow$	Prec $\uparrow$
w/o detection loss	42.3	52.4
w/o shape loss	58.7	73.7
full model	<b>62.3</b>	<b>77.7</b>

Table 5: **Ablation study on the KITTI dataset.** We analyze the contributions of the detection loss and the shape loss.

in Eq. 7), the shape loss (second term in Eq. 6 and first term in Eq. 7) and the Chamfer distance loss (CD loss, first term in Eq. 6) and observe all of them can improve the tracking performance. Among them, the proposed shape loss plays a far more important role than the Chamfer distance loss. We also observe applying object detection significantly boosts performance in the KITTI dataset given the noisy point cloud inputs.

#### 4.4. Qualitative Analysis

Figure 6 compares our reconstruction results with the baseline on the Waymo dataset. For the baseline, we use the LiDAR-SOT [32] to aggregate the point clouds over time, and apply the DeepSDF on the aggregated points to reconstruct shape at once. Figure 6 shows that our method produces more accurate shapes compared to the baseline. Due to the shape prior and the online adaptation mechanism, even when the input is sparse and partial, our method is still able to produce an acceptable shape.

## 5. Discussion

**Conclusion** In this paper, we present a novel and unified framework for object tracking and shape reconstruction in the wild. We propose to leverage the continuity and redundancy in video data with a differentiable shape model. Specifically, we utilize a DeepSDF model to simultaneously perform object tracking and 3D reconstruction. During the tracking process, we adapt shape model based on new observation to improve the shape quality, which leads to improvement on tracking, and vice versa. We also demonstrate that the results on both Waymo and KITTI datasets outperform state-of-the-art methods by a large margin.

**Limitations and future work** We describe two limitations of our method: (i) Since we have to focus on both object tracking and shape reconstruction, shapes can not be fully fitted to the observation at current time step. Once we overfit the shape to a specific frame, it is difficult to generalize to subsequent novel views. Hence, we have to maintain a relatively smooth shape during online tracking. In the future, other techniques can be introduced to preserve high-frequency details without loss of tracking accuracy. (ii) We focus on mainly “Car” category in this paper on the major tracking benchmarks. Future work aims to collect tracking datasets on other categories and implement a joint tracking and reconstruction model for general objects.

Table 6: Symbols used in this work.

Symbol	Definition
$\mathbf{T} \in SE(3)$	Transformation from the world frame to the LiDAR frame.
$\mathbf{b} = \{h, w, l\}$	Dimensions of the template 3D bounding box.
$\mathbf{P}_t$	Input point cloud at time $t$ .
$\mathbf{X}_t(\mathbf{T}) = \{\mathbf{x} \in \mathbf{P}_t   \mathbf{T}\mathbf{x} \leq \mathbf{b}\}$	Points inside 3D tracking bounding box posed by $\mathbf{T}$ at time $t$ .
$\mathbf{x} \in \mathbf{X}$	A point in a set of points $\mathbf{X}$ .
$\mathbf{z}$	Shape code of DeepSDF.
$s$	SDF value.
	Parameters of the DeepSDF model.
$\Gamma : \mathbf{X} \rightarrow 2^{\mathbf{X}}$	A selector function that samples points from a set of points $\mathbf{X}$ .
$\mathbf{H}_t = \Gamma(\{\mathbf{x}   \mathbf{x} \in \mathbf{X}_0 \cup \mathbf{X}_1 \cup \dots \cup \mathbf{X}_{t-1}\})$	Some subset of all previously tracked points.
$\phi(\mathbf{X}, \mathbf{Y}) = \sum_{\mathbf{x} \in \mathbf{X}} \min_{\mathbf{y} \in \mathbf{Y}} \ \mathbf{x} - \mathbf{y}\ _2^2$	Single-sided Chamfer distance between two sets of points $\mathbf{X}$ and $\mathbf{Y}$ .

## A. List of Symbols

We show all symbols used in this work in Table 6.

## B. Implementation Details

**Network architecture.** We adapt DeepSDF as our shape model. Specifically, we reduce the MLP from 8 layers to 5 layers. Moreover, since the SDF we use is not truncated, we remove the final tanh in DeepSDF. The dimension of the latent shape code is 512. For the pre-training of the shape model, we employ the Adam optimizer with an initial learning rate of  $1 \times 10^{-4}$  and a batch size of 128. The training process takes 16 epochs in total.

**Ground removing.** In experiments, we find that ground removing is necessary for our method. This is due to the ShapeNet dataset, which is utilized to pre-train our shape model, does not contain any ground point cloud. Therefore, the ground point cloud in the Waymo and the KITTI dataset is a huge domain gap that leads to poor reconstruction performance, which in turn degrades tracking performance. In experiments, we use the same algorithm used by LiDAR-SOT, but with more aggressive parameters to remove the ground more cleanly. The clean point cloud after ground removing is used for both tracking and reconstruction.

**Normalized coordinate.** Since the CAD models provided by the ShapeNet dataset are normalized to a unit cube, we also perform tracking and reconstruction in a normalized coordinate. In experiments, the input point clouds in the Waymo and the KITTI datasets are normalized based on the given and fixed object size.

**Selector function.** There are three choices to aggregate the historical points: only the previous frame observation, the combination of the first frame observation and previous

frame observation, and all previous observations. Among different sources of observation, the first frame point cloud is the most accurate since there is no error in pose estimation, but the distribution of point cloud may differ a lot from the current frame. In contrast, the distribution of the previous frame point cloud is more similar to the target point cloud since it is temporally closer. And the aggregated point cloud is the most complete observation but contains the most noise.

**Chamfer distance loss.** The Chamfer distance loss is utilized to help the pose estimation. Different from the shape loss which uses an implicit shape to optimize pose, the Chamfer distance loss applies on the raw point cloud and therefore can capture finer details of the object shape.

## References

- [1] Panos Achlioptas, Olga Diamanti, Ioannis Mitliagkas, and Leonidas Guibas. Learning representations and generative models for 3d point clouds. In *International conference on machine learning*, pages 40–49, 2018. 2
- [2] Timur Bagautdinov, Chenglei Wu, Jason Saragih, Pascal Fua, and Yaser Sheikh. Modeling facial geometry using compositional vaes. In *Proceedings of the IEEE Conference on Computer Vision and Pattern Recognition*, pages 3877–3886, 2018. 2
- [3] Erkan Baser, Venkateshwaran Balasubramanian, Prarthana Bhattacharyya, and Krzysztof Czarnecki. Fantrack: 3d multi-object tracking with feature association network. In *2019 IEEE Intelligent Vehicles Symposium (IV)*, pages 1426–1433, 2019. 2
- [4] Florian Chabot, Mohamed Chaouch, Jaonary Rabarisoa, Céline Teulière, and Thierry Chateau. Deep manta: A coarse-to-fine many-task network for joint 2d and 3d vehicle analysis from monocular image. In *Proceedings of the IEEE conference on computer vision and pattern recognition*, pages 2040–2049, 2017. 2
- [5] Rohan Chabra, Jan E Lenssen, Eddy Ilg, Tanner Schmidt, Julian Straub, Steven Lovegrove, and Richard Newcombe. Deep local shapes: Learning local sdf priors for detailed 3d reconstruction. In *European Conference on Computer Vision*, pages 608–625, 2020. 1
- [6] Angel X Chang, Thomas Funkhouser, Leonidas Guibas, Pat Hanrahan, Qixing Huang, Zimo Li, Silvio Savarese, Manolis Savva, Shuran Song, Hao Su, et al. Shapenet: An information-rich 3d model repository. *arXiv preprint arXiv:1512.03012*, 2015. 1, 2, 3, 5
- [7] Zhiqin Chen and Hao Zhang. Learning implicit fields for generative shape modeling. In *Proceedings of the IEEE/CVF Conference on Computer Vision and Pattern Recognition*, pages 5939–5948, 2019. 1, 2
- [8] Christopher B Choy, Danfei Xu, JunYoung Gwak, Kevin Chen, and Silvio Savarese. 3d-r2n2: A unified approach for single and multi-view 3d object reconstruction. In *European conference on computer vision*, pages 628–644, 2016. 2
- [9] Angela Dai, Angel X Chang, Manolis Savva, Maciej Halber, Thomas Funkhouser, and Matthias Nießner. Scannet: Richly-annotated 3d reconstructions of indoor scenes. In *Proceedings of the IEEE Conference on Computer Vision and Pattern Recognition*, pages 5828–5839, 2017. 1
- [10] Michaël Defferrard, Xavier Bresson, and Pierre Vandergheynst. Convolutional neural networks on graphs with fast localized spectral filtering. *arXiv preprint arXiv:1606.09375*, 2016. 2
- [11] Jiajun Deng, Shaoshuai Shi, Peiwei Li, Wengang Zhou, Yanyong Zhang, and Houqiang Li. Voxel R-CNN: towards high performance voxel-based 3d object detection. In *AAAI*, pages 1201–1209, 2021. 6
- [12] Shivam Duggal, Zihao Wang, Wei-Chiu Ma, Sivabalan Manivasagam, Justin Liang, Shenlong Wang, and Raquel Urtasun. Secrets of 3d implicit object shape reconstruction in the wild. *arXiv preprint arXiv:2101.06860*, 2021. 2
- [13] Francis Engelmann, Jörg Stückler, and Bastian Leibe. Joint object pose estimation and shape reconstruction in urban street scenes using 3d shape priors. In *German Conference on Pattern Recognition*, pages 219–230, 2016. 2, 3
- [14] Zheng Fang, Sifan Zhou, Yubo Cui, and Sebastian Scherer. 3d-siamrpn: An end-to-end learning method for real-time 3d single object tracking using raw point cloud. *IEEE Sensors Journal*, 2020. 2
- [15] Zheng Fang, Sifan Zhou, Yubo Cui, and Sebastian A. Scherer. 3d-siamrpn: An end-to-end learning method for real-time 3d single object tracking using raw point cloud. *IEEE Sensors Journal*, 21:4995–5011, 2021. 6
- [16] Qiaojun Feng, Yue Meng, Mo Shan, and Nikolay Atanasov. Localization and mapping using instance-specific mesh models. In *2019 IEEE/RSJ International Conference on Intelligent Robots and Systems (IROS)*, pages 4985–4991, 2019. 2
- [17] Andreas Geiger, Philip Lenz, and Raquel Urtasun. Are we ready for autonomous driving? the kitti vision benchmark suite. In *2012 IEEE Conference on Computer Vision and Pattern Recognition*, pages 3354–3361, 2012. 2, 5
- [18] Kyle Genova, Forrester Cole, Avneesh Sud, Aaron Sarna, and Thomas A. Funkhouser. Local deep implicit functions for 3d shape. In *CVPR*, pages 4856–4865, 2020. 2
- [19] Silvio Giancola, Jesus Zarzar, and Bernard Ghanem. Leveraging shape completion for 3d siamese tracking. In *Proceedings of the IEEE/CVF Conference on Computer Vision and Pattern Recognition*, pages 1359–1368, 2019. 2, 5, 6
- [20] Rohit Girdhar, David F Fouhey, Mikel Rodriguez, and Abhinav Gupta. Learning a predictable and generative vector representation for objects. In *European Conference on Computer Vision*, pages 484–499, 2016. 2
- [21] Amos Gropp, Lior Yariv, Niv Haim, Matan Atzmon, and Yaron Lipman. Implicit geometric regularization for learning shapes. *arXiv preprint arXiv:2002.10099*, 2020. 2
- [22] Hou-Ning Hu, Qi-Zhi Cai, Dequan Wang, Ji Lin, Min Sun, Philipp Krahenbuhl, Trevor Darrell, and Fisher Yu. Joint monocular 3d vehicle detection and tracking. In *Proceedings of the IEEE/CVF International Conference on Computer Vision*, pages 5390–5399, 2019. 2
- [23] Chiyu Jiang, Avneesh Sud, Ameesh Makadia, Jingwei Huang, Matthias Nießner, Thomas Funkhouser, et al. Local implicit grid representations for 3d scenes. In *Proceedings of the IEEE/CVF Conference on Computer Vision and Pattern Recognition*, pages 6001–6010, 2020. 1
- [24] Lei Ke, Shichao Li, Yanan Sun, Yu-Wing Tai, and Chi-Keung Tang. Gsnet: Joint vehicle pose and shape reconstruction with geometrical and scene-aware supervision. In *European Conference on Computer Vision*, pages 515–532, 2020. 2, 3
- [25] Amit P. S. Kohli, Vincent Sitzmann, and Gordon Wetzstein. Inferring semantic information with 3d neural scene representations. *CoRR*, abs/2003.12673, 2020. 2
- [26] Jason Ku, Melissa Mozifian, Jungwook Lee, Ali Harakeh, and Steven L Waslander. Joint 3d proposal generation and object detection from view aggregation. In *2018 IEEE/RSJ International Conference on Intelligent Robots and Systems (IROS)*, pages 1–8, 2018. 2
- [27] Abhijit Kundu, Yin Li, and James M Rehg. 3d-rcnn: Instance-level 3d object reconstruction via render-and-compare. In

- Proceedings of the IEEE conference on computer vision and pattern recognition*, pages 3559–3568, 2018. 2
- [28] Wenjie Luo, Bin Yang, and Raquel Urtasun. Fast and furious: Real time end-to-end 3d detection, tracking and motion forecasting with a single convolutional net. In *Proceedings of the IEEE conference on Computer Vision and Pattern Recognition*, pages 3569–3577, 2018. 2
- [29] Lars Mescheder, Michael Oechsle, Michael Niemeyer, Sebastian Nowozin, and Andreas Geiger. Occupancy networks: Learning 3d reconstruction in function space. In *Proceedings of the IEEE/CVF Conference on Computer Vision and Pattern Recognition*, pages 4460–4470, 2019. 1, 2
- [30] Ben Mildenhall, Pratul P. Srinivasan, Matthew Tancik, Jonathan T. Barron, Ravi Ramamoorthi, and Ren Ng. Nerf: Representing scenes as neural radiance fields for view synthesis. In *ECCV*, pages 405–421, 2020. 2
- [31] Michael Niemeyer, Lars M. Mescheder, Michael Oechsle, and Andreas Geiger. Differentiable volumetric rendering: Learning implicit 3d representations without 3d supervision. In *CVPR*, pages 3501–3512, 2020. 2
- [32] Ziqi Pang, Zhichao Li, and Naiyan Wang. Model-free vehicle tracking and state estimation in point cloud sequences. *IROS*, 2021. 2, 5, 6, 8
- [33] Jeong Joon Park, Peter Florence, Julian Straub, Richard Newcombe, and Steven Lovegrove. DeepSDF: Learning continuous signed distance functions for shape representation. In *Proceedings of the IEEE/CVF Conference on Computer Vision and Pattern Recognition*, pages 165–174, 2019. 1, 2, 3
- [34] Charles R Qi, Wei Liu, Chenxia Wu, Hao Su, and Leonidas J Guibas. Frustum pointnets for 3d object detection from rgb-d data. In *Proceedings of the IEEE conference on computer vision and pattern recognition*, pages 918–927, 2018. 2
- [35] Charles R Qi, Hao Su, Kaichun Mo, and Leonidas J Guibas. Pointnet: Deep learning on point sets for 3d classification and segmentation. In *Proceedings of the IEEE conference on computer vision and pattern recognition*, pages 652–660, 2017. 2
- [36] Haozhe Qi, Chen Feng, Zhiguo Cao, Feng Zhao, and Yang Xiao. P2b: Point-to-box network for 3d object tracking in point clouds. In *Proceedings of the IEEE/CVF Conference on Computer Vision and Pattern Recognition*, pages 6329–6338, 2020. 2, 6
- [37] Shunsuke Saito, Zeng Huang, Ryota Natsume, Shigeo Morishima, Angjoo Kanazawa, and Hao Li. Pifu: Pixel-aligned implicit function for high-resolution clothed human digitization. In *Proceedings of the IEEE/CVF International Conference on Computer Vision*, pages 2304–2314, 2019. 2
- [38] Shunsuke Saito, Tomas Simon, Jason Saragih, and Hanbyul Joo. Pifuhd: Multi-level pixel-aligned implicit function for high-resolution 3d human digitization. In *Proceedings of the IEEE/CVF Conference on Computer Vision and Pattern Recognition*, pages 84–93, 2020. 2
- [39] Abhijeet Sheno, Mihir Patel, JunYoung Gwak, Patrick Goebel, Amir Sadeghian, Hamid Reza Tofighi, Roberto Martin-Martin, and Silvio Savarese. Jrmot: A real-time 3d multi-object tracker and a new large-scale dataset. *arXiv preprint arXiv:2002.08397*, 2020. 2
- [40] Martin Simon, Karl Amende, Andrea Kraus, Jens Honer, Timo Samann, Hauke Kaulbersch, Stefan Milz, and Horst Michael Gross. Complexer-yolo: Real-time 3d object detection and tracking on semantic point clouds. In *Proceedings of the IEEE/CVF Conference on Computer Vision and Pattern Recognition Workshops*, pages 0–0, 2019. 2
- [41] Vincent Sitzmann, Julien N. P. Martel, Alexander W. Bergman, David B. Lindell, and Gordon Wetzstein. Implicit neural representations with periodic activation functions. *CoRR*, abs/2006.09661, 2020. 2
- [42] Vincent Sitzmann, Michael Zollhöfer, and Gordon Wetzstein. Scene representation networks: Continuous 3d-structure-aware neural scene representations. In *NeurIPS 2019*, pages 1119–1130, 2019. 2
- [43] Xibin Song, Peng Wang, Dingfu Zhou, Rui Zhu, Chenye Guan, Yuchao Dai, Hao Su, Hongdong Li, and Ruigang Yang. Apollocar3d: A large 3d car instance understanding benchmark for autonomous driving. In *Proceedings of the IEEE/CVF Conference on Computer Vision and Pattern Recognition*, pages 5452–5462, 2019. 2
- [44] Pei Sun, Henrik Kretschmar, Xerxes Dotiwalla, Aurelien Chouard, Vijaysai Patnaik, Paul Tsui, James Guo, Yin Zhou, Yuning Chai, Benjamin Caine, et al. Scalability in perception for autonomous driving: Waymo open dataset. In *Proceedings of the IEEE/CVF Conference on Computer Vision and Pattern Recognition*, pages 2446–2454, 2020. 2, 5
- [45] Alex Trevisan and Bo Yang. GRF: learning a general radiance field for 3d scene representation and rendering. *CoRR*, abs/2010.04595, 2020. 2
- [46] Nanyang Wang, Yinda Zhang, Zhuwen Li, Yanwei Fu, Wei Liu, and Yu-Gang Jiang. Pixel2mesh: Generating 3d mesh models from single rgb images. In *Proceedings of the European Conference on Computer Vision (ECCV)*, pages 52–67, 2018. 2
- [47] Xinshuo Weng, Jianren Wang, David Held, and Kris Kitani. 3d multi-object tracking: A baseline and new evaluation metrics. *arXiv preprint arXiv:1907.03961*, 2020. 2
- [48] Zhirong Wu, Shuran Song, Aditya Khosla, Fisher Yu, Linguang Zhang, Xiaoou Tang, and Jianxiong Xiao. 3d shapenets: A deep representation for volumetric shapes. In *Proceedings of the IEEE conference on computer vision and pattern recognition*, pages 1912–1920, 2015. 2
- [49] Qiangeng Xu, Weiyue Wang, Duygu Ceylan, Radomir Mech, and Ulrich Neumann. Disn: Deep implicit surface network for high-quality single-view 3d reconstruction. *arXiv preprint arXiv:1905.10711*, 2019. 2, 5
- [50] Yaoqing Yang, Chen Feng, Yiru Shen, and Dong Tian. Foldingnet: Interpretable unsupervised learning on 3d point clouds. *arXiv preprint arXiv:1712.07262*, 2(3):5, 2017. 2
- [51] Sergey Zakharov, Wadim Kehl, Arjun Bhargava, and Adrien Gaidon. Autolabeling 3d objects with differentiable rendering of sdf shape priors. In *Proceedings of the IEEE/CVF Conference on Computer Vision and Pattern Recognition*, pages 12224–12233, 2020. 2
- [52] Jesus Zarzar, Silvio Giancola, and Bernard Ghanem. Efficient bird eye view proposals for 3d siamese tracking. *arXiv e-prints*, pages arXiv–1903, 2019. 2

- [53] Muhammad Zeeshan Zia, Michael Stark, and Konrad Schindler. Are cars just 3d boxes?-jointly estimating the 3d shape of multiple objects. In *Proceedings of the IEEE Conference on Computer Vision and Pattern Recognition*, pages 3678–3685, 2014. 2
- [54] Chaoda Zheng, Xu Yan, Jiantao Gao, Weibing Zhao, Wei Zhang, Zhen Li, and Shuguang Cui. Box-aware feature enhancement for single object tracking on point clouds. In *Proceedings of the IEEE/CVF International Conference on Computer Vision*, pages 13199–13208, 2021. 6